Plaque Tissue Characterization and Classification in Ultrasound Carotid Scans: A Paradigm for Vascular Feature Amalgamation

U. Rajendra Acharya, M. Muthu Rama Krishnan, S. Vinitha Sree, João Sanches, Shoaib Shafique, Andrew Nicolaides, Luís Mendes Pedro, and Jasjit S. Suri

***Abstract*—The selection of carotid atherosclerosis patients for surgery or stenting is a crucial task in atherosclerosis disease management. In order to select only those symptomatic cases who need surgery, we have, in this work, presented a computer-aided diagnostic technique to effectively classify symptomatic and asymptomatic plaques from B-mode ultrasound carotid images. We extracted several grayscale features that quantify the textural differences inherent in the manually delineated plaque regions and selected the most significant among these extracted features. These features, along with the degree of stenosis (DoS), were used to train and test a support vector machine (SVM) classifier using threefold stratified cross-validation using a data set consisting of 160 (50 symptomatic and 110 asymptomatic) images. Using 32 features in an SVM classifier with a polynomial kernel of order 1, we obtained the best accuracy of 90.66%, sensitivity of 83.33%, and specificity of 95.39%. The DoS was found to be a valuable feature in addition to other texture-based features. We have also proposed the plaque risk index (PRI) made up of a combination of significant features such that the PRI has unique ranges for both plaque classes. *PRI* can be used in monitoring the variations in features over a period of time which will provide evidence on how and which features change as asymptomatic plaques become symptomatic.**

***Index Terms*—Atherosclerosis, carotid ultrasound, index, plaque, stenosis, texture.**

Manuscript received April 1, 2012; revised August 3, 2012; accepted August 10, 2012. Date of publication October 23, 2012; date of current version December 29, 2012. The Associate Editor coordinating the review process for this paper was Dr. Domenico Grimaldi.

U. Rajendra Acharya is with the Department of Electronics and Computer Engineering, Ngee Ann Polytechnic, 599489 Singapore, and also with the Department of Biomedical Engineering, Faculty of Engineering, University of Malaya, 50603 Kuala Lumpur, Malaysia (e-mail: aru@np.edu.sg).

M. M. Rama Krishnan is with the Department of Electronics and Computer Engineering, Ngee Ann Polytechnic, 599489 Singapore (e-mail: mkm2@np.edu.sg).

S. Vinitha Sree is with Global Biomedical Technologies Inc., Roseville, CA 95661 USA (e-mail: vinitha.sree@gmail.com).

J. Sanches is with the Department of Electrical and Computer Engineering, Instituto Superior Tecnico, Lisboa 1049-001, Portugal (e-mail: jmrs@isr.ist.utl.pt).

S. Shafique is with CorVasc MDs, Indianapolis, IN 46260 USA (e-mail: endovsolutions@aol.com).

A. Nicolaides is with the Vascular Screening and Diagnostic Centre, Imperial College, SW7 2AZ London, U.K., and also with the Department of Biological Sciences, University of Cyprus, Nicosia, 20537-1678 Cyprus (e-mail: a.nicolaides@imperial.ac.uk).

L. M. Pedro is with the Cardiovascular Institute and the Lisbon University Medical School, Hospital de Santa Maria, Lisbon 1600-190, Portugal (e-mail: lmendespedro@clix.pt).

J. S. Suri is with AtheroPoint LLC, Roseville, CA 95661 USA, and also with the Department of Biomedical Engineering, Idaho State University, Pocatello, ID 83209 USA (e-mail: jsuri@comcast.net).

Color versions of one or more of the figures in this paper are available online at http://ieeexplore.ieee.org.

Digital Object Identifier 10.1109/TIM.2012.2217651

I. Introduction

CAROTID ATHEROSCLEROSIS is a primary cause of cardiovascular diseases like stroke and heart attack. The World Health Organization estimates that, by 2030, almost 23.6 million people will die mostly from heart disease and stroke [1]. It has been observed that symptomatic patients [who have had retinal or hemispheric symptoms such as stroke, transient ischemic attack (TIA), and amaurosis fugax (AF)] have more frequent plaque ruptures that cause life-threatening embolization. Plaque rupture was seen in 74% of symptomatic plaques and in only 32% of plaques from asymptomatic patients [2]. The common treatment options such as carotid artery stenting and carotid endarterectomy (CEA) carry considerable risk to the patient [3]. Therefore, techniques are needed to effectively select only those symptomatic patients at risk of stroke for these procedures. When the degree of stenosis (DoS) based on the European Carotid Surgery Trial criteria [4]–[6] was greater than 80%, CEA was prescribed [6]. However, there is evidence that plaques with relatively low stenosis degree may produce symptoms [7] and the majority of asymptomatic patients with highly stenotic atherosclerotic plaques remain asymptomatic [8]. Therefore, there is a need for additional plaque characterization techniques that can detect symptomatic and asymptomatic groups.

The common carotid artery is routinely used to detect the presence of plaques. Ultrasound is the most preferred modality for the evaluation of the structural aspects of atheromatous plaques such as the presence of surface ulceration, echogenicity, and heterogeneity of the plaque content [9], [10]. However, ultrasound is limited by low image resolution and artifacts. Computer-aided diagnostic (CAD) techniques using data mining frameworks can address these issues using preprocessing algorithms [11]–[13]. Thus, the primary objectives of this work are the following: 1) to develop a data mining-based plaque characterization and classification framework to classify plaques into symptomatic and asymptomatic types and 2) to develop an integrated index based on the significant grayscale features to more objectively classify plaques into the two classes. The protocol of the proposed technique is in line with several related studies in the literature [14]–[22]. These studies (see Section VII) have exploited the use of texture features in

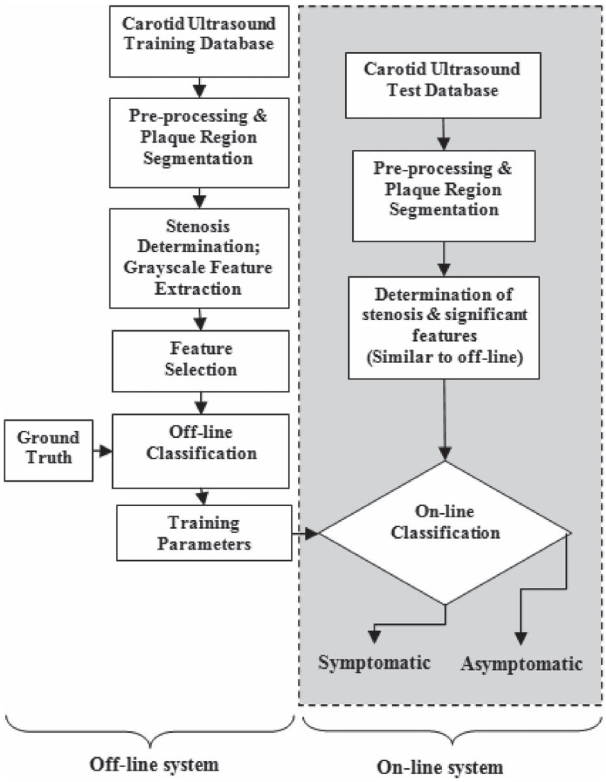

Fig. 1. Block diagram of the proposed CAD technique for plaque characterization.

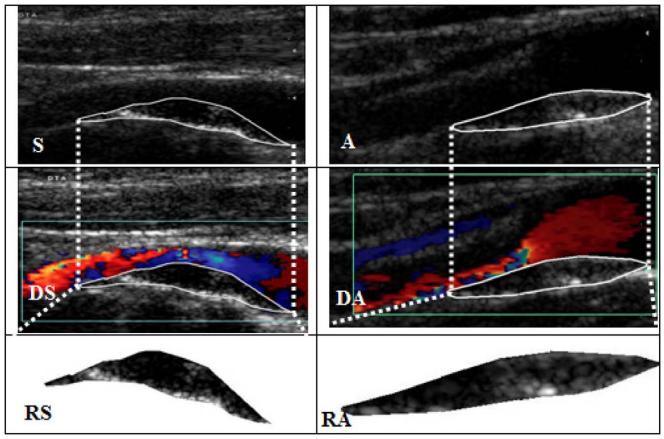

Fig. 2. Carotid (S) symptomatic and (A) asymptomatic plaque images. (DS and DA) Corresponding color Doppler images. (RS and RA) Corresponding extracted plaque region of interests (zoomed).

addition to other features. In our technique, we have studied the utility of several texture-based features described in Section III along with the DoS.

The proposed CAD system is shown in Fig. 1. It consists of an online system (shown on the right side of Fig. 1) which processes an incoming patient's test image. This system predicts the class label based on the transformation of the online grayscale feature vector by the training parameters determined by an offline learning system (shown on the left side of Fig. 1). The offline classification system is composed of a classification phase which produces the training parameters using the combination of offline training features and the respective offline ground-truth training class labels (0/1 for asymptomatic/symptomatic). The ground truth is based on the prior history of symptoms in the patient. In both systems, the grayscale features are several texture-based features from the manually segmented plaque regions of the input images. Significant features among the extracted ones are selected using the t-test. We evaluated the support vector machine (SVM) classifier as the offline learning classifier. The aforementioned CAD system was developed using a k-fold cross-validation protocol. The predicted class labels of the test images and the corresponding ground-truth labels (0/1) were compared to determine the performance measures such as sensitivity, specificity, accuracy, and positive predictive value (PPV).

II. Description of the Data

In this paper, we have used 160 plaques (110 asymptomatic plaques and 50 symptomatic ones). Approval from the Institutional Review Board and informed consent from patients were obtained prior to conducting the study. Images were acquired at the Instituto Cardiovascular de Lisboa, Lisbon, Portugal. A plaque was considered symptomatic when the subject experienced AF or focal transitory, reversible, or established neurological symptoms in the ipsilateral carotid territory in the previous six months. If there were no symptoms, the plaque was considered asymptomatic. Patients were selected consecutively through neurological consultation which included noninvasive examination with color-flow duplex scan of one or both carotids. HDI5000 Philips US machine, with an L12-5 scan probe (5–12-MHz broad-band linear array transducer) operating in B-mode, was used for image acquisition at 25 pixels/mm resolution. In order to ensure that images acquired under different conditions produce comparable and reproducible features, image normalization was carried out using the technique reported in [23]. The intensities of the resultant normalized image were linearly scaled so that the adventitia and blood intensities were in the ranges of 190–195 and 0–5, respectively. A region of interest (ROI) containing the plaque was manually delineated from the normalized images by drawing around the structure of the plaque. The resultant ROI was evenly resampled and smoothed using spline interpolation. Matlab software was used for normalization and ROI selection.

In Fig. 2, (S) and (A) show typical symptomatic and asymptomatic images that are cropped to omit the patient details in order to conform to the Health Insurance Portability and Accountability Act (HIPAA) requirements. (DS) and (DA) show the corresponding color Doppler images. (RS) and (RA) show the respective zoomed ROIs. The nature of the atherosclerotic disease is focused on the vessel wall that specifically changes the morphology of the lumen–intima interface from slow gradual lipid formation and maturing into hard plaque or loose island of hemorrhage [24]. Therefore, the young and old plaques are all focused toward the vessel disease which yields the information in the form of echogenicity in the ultrasound image [25]. This focused ROI constitutes less than 25% of the image frame, and hence, our goal is to characterize plaque in this regional information.

III. Grayscale Feature Extraction and Selection

In the ultrasound images, heterogeneous plaques have more than 20% of the overall plaque area differing from the rest of the plaque by two or more echogenicity grades [26]. It was shown that patients with 60% to 69% asymptomatic carotid stenosis with heterogeneous plaques had a higher incidence rate of late ipsilateral stroke, TIA, and progression to 70% stenosis than patients with homogeneous plaques [27]. Thus, characterizing these subtle differences in the image texture using grayscale features will help in symptomatic versus asymptomatic classification. In this section, brief descriptions of the various features used are given.

A. LBP

The local binary pattern (LBP) [26], [28], [29] was determined as a grayscale-invariant texture measure derived from the texture in a local neighborhood. In this paper, a rotation-invariant measure called $LBP_{P,R}$ using uniformity measure U was calculated. Only patterns with $U \leq 2$ were assigned the LBP code as depicted in the following:

$$LBP_{P,R}(x) = \begin{cases} \sum_{p=0}^{P-1} s(g_p - g_c) & \text{if} \quad U(x) \leq 2 \\ P+1 & \text{otherwise} \end{cases} \tag{1}$$

where $s(x) = \begin{cases} 1, x \geq 0 \\ 0, x < 0 \end{cases}$.

To include the local image texture contrast, we used a rotation-invariant measure of local variance given by

$$VAR_{P,R} = \frac{1}{P}\sum_{p=0}^{P-1}(g_p - \mu)^2, \text{ where } \mu = \frac{1}{P}\sum_{p=0}^{P-1} g_p. \tag{2}$$

In this paper, we determined the three LBP images over different scales ($R = 1$, 2, and 3 with the corresponding pixel count $P = 8$, 16, and 24, respectively). The mean ($LBP1-3$), variance ($LBP4-6$), and local contrast ($LBP7-9$) of these three images were used as texture descriptors.

B. FGLCM

The boundaries separating the various regions in an image are generally not sharp. Therefore, we used fuzzy features to quantify the textural changes. The fuzzy gray-level co-occurrence matrix ($FGLCM$) [30] of an image I of size $L \times L$ is given by

$$F_d(m,n) = [f_{mn}]_{L\times L} \tag{3}$$

where f_{mn} corresponds to the frequency of occurrence of a gray value "around m" separated from another pixel, with a gray value "around n," by a distance d in a specific direction θ. Herein, we used the rotational invariant co-occurrence matrix obtained by averaging the four symmetrical fuzzy co-occurrence matrices computed with $\theta = 0°$, 45°, 90°, 135°, and $d = 20$ to calculate the following texture features. The pyramidal membership function $\mu_{\tilde{m}I(x,y),\tilde{n}I(x,y\pm d)}$ used to build these matrices had a support of 11×11 pixels.

$$\text{GLCM Energy} : EneT = \sum_m \sum_n [F_d(m,n)]^2 \tag{4}$$

$$\text{GLCM Contrast} : ConT = \sum_m \sum_n (m-n)^2 F_d(m,n) \tag{5}$$

$$\text{GLCM Homogeneity} : HOM = \sum_m \sum_n \frac{F_d(m,n)}{1+(m-n)^2} \tag{6}$$

$$\text{GLCM Symmetry} : SYM = \sum_m \sum_n [F_d(m,n) - F_d(n,m)]^2 \tag{7}$$

$$\text{GLCM Correlation} : CORR = \frac{\sum_{m=0}^{N-1}\sum_{n=0}^{N-1}(m,n)F_d(m,n) - \mu_m\mu_n}{\sigma_m\sigma_n} \tag{8}$$

where

$$\mu_m = \sum mF_d(m,n), \quad \sigma_m^2 = \sum m^2 F_d(m,n) - \mu_m^2$$
$$\mu_n = \sum nF_d(m,n), \quad \sigma_n^2 = \sum n^2 F_d(m,n) - \mu_n^2$$

$$\text{GLCM Entropy} : EntT = -\sum_m \sum_n F_d(m,n).\ln F_d(m,n) \tag{9}$$

$$\text{GLCM Moments } m_1, m_2, m_3 \text{ and } m_4 :_{m_g} = \sum_m \sum_n (m-n)^g F_d(m,n). \tag{10}$$

Difference statistics is defined as "the distribution of the probability that the gray-level difference is k between the points separated by δ in an image" [31]. The difference statistics vector can be obtained from FGLCM as [32]

$$F_\delta(k) = \sum_m \sum_{\substack{n \\ |m-n|=k}} F_d(m,n) \tag{11}$$

$$\text{Angular Second Moment} : A2M = \sum_{k=0}^{N-1} F_\delta(k)^2 \tag{12}$$

$$\text{Mean} : DM = \sum_{k=0}^{N-1} k_\delta(k). \tag{13}$$

$$\text{Difference statistics entropy} : EntD = -\sum_{k=0}^{N-1} F_\delta(k)\ln F_\delta(k) \tag{14}$$

$$\text{Difference statistics contrast} : ConD = \sum_{k=0}^{N-1} k^2 F_\delta(k) \tag{15}$$

$$\text{Difference statistics energy} : EneD = \sum_{k=0}^{N-1} [F_\delta(k)]^2 \tag{16}$$

where $k = 0, 1, \ldots N-1$, N is the number of grayscale level [30], and δ is $d = (\Delta m, \Delta n)$.

C. FRLM

The fuzzy run length matrix $(FRLM)$ $F_\theta(m,n)$ [32] contains all the elements which represent the frequency that j pixels with gray-level intensity i continue in the direction θ. The direction θ is set as 0°, 45°, 90°, or 135°. In this paper, we calculated the following features based on the run length matrix

$$SRE = \frac{\sum_m \sum_n \frac{F_\theta(m,n)}{n^2}}{\sum_m \sum_n F_\theta(m,n)} \tag{17}$$

Long Run Emphasis : LRE

$$= \frac{\sum_m \sum_n n^2 F_\theta(m,n)}{\sum_m \sum_n F_\theta(m,n)} \tag{18}$$

Gray-Level Nonuniformity : $GLNU$

$$= \frac{\sum_m \left\{ \sum_n F_\theta(m,n) \right\}^2}{\sum_m \sum_n F_\theta(m,n)} \tag{19}$$

Run Length Nonuniformity : $RLNU$

$$= \frac{\sum_n \left\{ \sum_m F_\theta(m,n) \right\}^2}{\sum_m \sum_n F_\theta(m,n)} \tag{20}$$

Run Percentage : RP

$$= \frac{\sum_m \sum_n F_\theta(m,n)}{A} \tag{21}$$

where A is the area of the image. The index i runs over the gray-level values, and the index j runs over the run length.

D. Trace Transform

The ultrasound images may be slightly different due to various acquisition angles and gain settings. Therefore, we used trace transform to obtain features which are invariant to rotation, translation, and scaling [33]. T, the *trace functional*, is first applied along lines tracing the image in order to transform the image into the $(\phi; p; t)$ parameter space and to obtain the trace transform matrix. Next, P, the *diametrical functional*, is applied on the matrix (p-direction) to get a string. Finally, a *circus functional*Φ is applied along the string (ϕ-direction) to obtain a single-valued *triple feature* [33]. The triple feature $\Pi(f, I)$ of image $f(x, y)$ in image space I can be defined as

$$\Pi(f, I) = \Phi\left(P\left(T\left(f(I; p, \phi, t)\right)\right)\right). \tag{22}$$

In this paper, we calculated two triple features (23) and (24) using the invariant functionals IF_1, IF_2, IF_3 defined in [33].

$$\Pi_1 = (T \to IF_1, P \to IF_2, \Phi \to IF_3) \tag{23}$$

$$\Pi_2 = (T \to IF_3, P \to IF_2, \Phi \to IF_1) \tag{24}$$

where Π_1 is the normalized version of the triple feature formed by using IF_1, IF_2, and IF_3 for functionals T, P, and Φ, respectively, in (22). Π_2 uses IF_3, IF_2, and IF_1 for functionals T, P, and Φ, respectively.

E. HOS Features

Higher order spectrum (HOS) analysis is a powerful tool for the nonlinear dynamical analysis of physiological signals which are generally nonlinear, nonstationary, and non-Gaussian in nature [34], [35]. HOS is the spectral representation of moments and cumulants of the third and higher orders. Since the HOS of Gaussian signals is statistically zero, this analysis can separate a non-Gaussian signal from an additive mixture of independent non-Gaussian signals and Gaussian noise. Thus, HOS techniques provide high noise immunity. The images were first subjected to the Radon transform [36] before the aforementioned HOS features were extracted. In this paper, we calculated the bispectrum $B(f_1, f_2)$, which is the third-order cumulant generating function. It is given by

$$B(f_1, f_2) = E\left[X(f_1)X(f_2)X(f_1 + f_2)\right] \tag{25}$$

where $X(f)$ is the Fourier transform of the signal $x(nT)$, n is an integer index, T is the sampling interval, and $E[.]$ is the expectation operator. The bispectrum gives the cross-correlation between frequency components in a 2-D frequency plot. The following H parameters, calculated in this work, are related to the moments of the bispectrum. The sum of the logarithmic amplitudes of the bispectrum H_1 is given by

$$H_1 = \sum_\Omega \log\left(|B(f_1, f_2)|\right). \tag{26}$$

The sum of the logarithmic amplitudes of the diagonal elements in the bispectrum H_2 is given by

$$H_2 = \sum_\Omega \log\left(|B(f_k, f_k)|\right). \tag{27}$$

The first-order spectral moment of the amplitudes of the diagonal elements of the bispectrum H_3 is

$$H_3 = \sum_{k=1}^{N} k \log\left(|B(f_k, f_k)|\right) \tag{28}$$

$$H_4 = \sum_{k=1}^{N} (k - H_3)^2 \log\left(|B(f_k, f_k)|\right). \tag{29}$$

All the aforementioned features are defined over a principal domain Ω [35]. We also calculated the bispectral phase entropy

$$P_h = \sum_n p(\psi_n) log p(\psi_n) \tag{30}$$

where

$$p(\psi_n) = \frac{1}{L} \sum_\Omega l\left(\phi\left(B(f_1, f_2)\right) \in \psi_n\right) \tag{31}$$

$$\psi_n = \left\{\phi \middle| -\pi + 2\pi n/N \le \phi < -\pi + 2\pi(n+1)/N\right\}, \quad n = 0, 1, \ldots, N-1 \tag{32}$$

where L is the number of points within the region Ω, ϕ is the phase angle of the bispectrum, and $l(.)$ is an indicator function which gives a value of 1 when the phase angle is within the

range depicted by Ψ_n in (32). We extracted the aforementioned features for every 1° of the Radon transform between 0 and 180°.

F. FS Descriptor

In order to quantify the changes in the image edges, we chose the Fourier spectrum (FS) descriptor. The FS descriptors are coefficients of the discrete Fourier transform (DFT) of the complex vector $s(k)$ formed by K edge points in an image. It is given by

$$F(u) = \sum_{k=0}^{K-1} s(k) e^{-j2\pi uk/K}. \tag{33}$$

In this paper, we have used Fourier energy, which is the square of the DFT magnitude, as the FS descriptor. Fourier descriptors are not invariant to scaling and translation.

G. Other Features

Apart from these features, we also used the grayscale mean (GSM) of the histogram representing the distribution of pixel intensities. The percentile 40 $(P40)$ is the percentage of pixels with gray levels below 40 that can determine the amount of dark regions within the plaque. It provides an assessment of the echogenicity of the plaque and has been found to be a significant feature [37]. Several studies have indicated that the DoS may be a major determinant of stroke in both symptomatic and asymptomatic cases [4], [38], [39]. We quantified the DoS using color-flow duplex-scan criteria: cross-sectional area measurement combined with hemodynamic assessment [40].

H. Feature Ranking and Selection

All extracted features were checked for possibly highly correlated features. This process assists in removing any bias toward certain features which might afterward affect the classification procedure. Approaches based on *t-test*, divergence measure, and the Chernoff bound and Bhattacharya distance were used for feature ranking between the symptomatic and asymptomatic classes.

Independent Sample t-Test: We used the Student's *t-test* to assess whether the means of a feature from two classes are significantly different [41]. A low *p-value* ($< 0.01/0.05$) indicates that the feature is significant. All features had a normal distribution, which is a necessary condition for this test.

KL Divergence Measure: An approach which is based on the summation of the divergence measure for each feature between the symptomatic and asymptomatic cases was adopted for ranking the features. An advantage of using the Kullback–Leibler (KL) divergence function for inspecting feature separability is that it places no prior assumption on class-conditional densities and has a direct relation with the Bayes error [42], which can be defined by the following formula:

$$D_i(f_i) = \sum_{k=1}^{n_c} \sum_{l>k}^{n_c} \frac{\left(\sigma_{k,f_i} - \sigma_{l,f_i}\right)^2 \left(1 + \sigma_{k,f_i} + \sigma_{lf_i}\right)}{2\sigma_{k,f_i}\sigma_{l,f_i}} \tag{34}$$

where n_c is the number of classes and $\sigma_{k,f}$ and σ_{l,f_i} are the standard deviations of the feature for classes k and l, respectively. Next, the features are ranked in a descending order according to their corresponding divergence values. The features with the higher divergence are the most significant as they maximize the separability between the groups.

Chernoff Bound and Bhattacharya Distance: The minimum attainable classification error of the Bayes classifier [43] for two classes ω_1 and ω_2 can be written as

$$P_e = \int_{-\alpha}^{\alpha} \min\left[P(\omega_i)p(x|\omega_i), P(\omega_j)p(x|\omega_j)\right] dx. \tag{35}$$

However, an upper bound can be derived. The derivation is based on the inequality

$$\min[a, b] \leq a^s b^{1-s} \text{ for } a, b \geq 0, \text{ and } 0 \leq s \leq 1. \tag{36}$$

Combining (35) and (36), we get

$$P_e \leq P(\omega_i)^s P(\omega_j)^{1-s} \int_{-\alpha}^{\alpha} p(x|\omega_i)^{1-s} dx \equiv \epsilon_{CB}\ . \tag{37}$$

ϵ_{CB} is known as the Chernoff bound. The minimum bound can be computed by minimizing ϵ_{CB} with respect to s. A special form of the bound results for $s = 1/2$

$$P_e \leq \epsilon_{CB} = \sqrt{P(\omega_i)P(\omega_j)} \int_{-\alpha}^{\alpha} \sqrt{p(x|\omega_i)p(x|\omega_j)dx}. \tag{38}$$

For Gaussian distributions $N(\mu_i, \sum_i)$ and $N(\mu_j, \sum_j)$, we obtain

$$\epsilon_{CB} = \sqrt{P(\omega_i)P(\omega_j)}\exp(-B) \tag{39}$$

where

$$B = \frac{1}{8}(\mu_i - \mu_j)^T \left(\frac{\sum_i + \sum_j}{2}\right)^{-1} (\mu_i - \mu_j) + \frac{1}{2}\ln \frac{\left|\frac{\sum_i + \sum_j}{2}\right|}{\sqrt{|\sum_i|\left|\sum_j\right|}} \tag{40}$$

and $|\bullet|$ denotes the determinant of the respective matrix. The term B is the *Bhattacharya distance*, and it is used as a class separability measure. This was used for feature ranking.

IV. Classification

SVM

SVM is a supervised classifier whose main objective is to find a separating hyperplane that separates the training samples belonging to the two classes with a maximum margin between the hyperplane and the samples closest to the hyperplane (called the support vectors) [44], [45]. In this paper, we have evaluated

the SVM classifier with polynomial kernels of varying orders and the radial basis function (RBF) kernels.

Threefold stratified cross-validation data resampling technique was used to evaluate the classifiers. Herein, the data set is randomly split into three equal parts, each containing the same proportion of samples from each class. Two parts (106 images) are used for training the classifiers to obtain the classifier parameters that best relate the input feature set and the corresponding ground-truth class label (symptomatic or asymptomatic). During the testing phase, these training parameters are used to classify the remaining one part (54 images), and the resultant class labels are compared with the actual ground-truth class labels in order to calculate accuracy, sensitivity, specificity, and PPV. This process is repeated two more times, using a different part for testing each time, ensuring that no test image is in the training set. The averages of the performance measures obtained from the test set over all the three iterations are reported as the final performance measures.

V. PRI

We have empirically formulated a single integrated index, called the plaque risk index (PRI), which is a unique combination of the features in such a way that the index has a unique range for both the classes. PRI is more comprehendible to the physicians than the classifiers which are most times black boxes that directly output the class label. PRI can also be adequately monitored over time to better understand which features get affected as asymptomatic plaques become symptomatic. PRI is given by (41), where $\eta = -30$

$$PRI = \frac{\beta \times \chi}{(\alpha \times \gamma)10^{\eta}} \tag{41}$$

where

$$\alpha = H_1(180^\circ) \times H_2(135^\circ) \times H_1(135^\circ) \times H_4(180^\circ) \times P_e$$

$$\beta = LBP2 + LBP3 + LBP5 + LBP6 + LBP7 + LBP8 + LBP9$$

$$\chi = LRE \times A2M \times EntD \times EneT \times RLN \times EntT \times SRE \times M4 \times M2 \times ConT \times GNU \times DM \times ConD \times HOM \times CORR \times TT1 \times FS$$

$$\gamma = GSM \times P40 \times DoS.$$

VI. RESULTS

A. Feature Ranking and Selection

Among all three ranking methods, we observed that the KL divergence-based method provided higher accuracy (see Table II). In this method, the features are ranked in a descending order according to their corresponding divergence values. The features with the higher divergence are most significant. Table I summarizes the mean $\pm$ standard deviation (SD) of these significant features and the corresponding divergence value. Based on the divergence values, 36 features were ranked and chosen. In Table I Feature Set A, the features have been listed in descending rank order (LRE = rank 1; RP = rank 36).

TABLE I
RANKED FEATURES (MEAN±STANDARD DEVIATION) BASED ON DIVERGENCE VALUE

Features	Symptomatic (Mean ± SD)	Asymptomatic (Mean ± SD)	Divergence value
Feature Set A			
LRE	56.02±46.10	97.68±136.51	3.89
P_h	3.38±0.22	3.15±0.45	1.93
FS	$(1.33\pm1.36)\times10^{12}$	$(2.78\pm2.67)\times10^{12}$	1.78
LBP8	0.43±0.09	0.34±0.07	1.47
LBP5	0.38±0.10	0.29±0.07	1.31
LBP9	0.48±0.01	0.46±0.01	1.17
A2M	$(35.73\pm48.19)\times10^{06}$	$(67.06\pm86.83)\times10^{06}$	1.05
LBP6	0.47±0.02	0.44±0.02	0.94
LBP3	0.32±0.05	0.28±0.04	0.91
LBP2	0.19±0.05	0.15±0.04	0.88
EntD	39.95±38.71	64.25±58.07	0.63
$H_4(180°)$	$2.37\times10^{11}\pm4.84\times10^{10}$	$2.68\times10^{11}\pm6.22\times10^{10}$	0.44
EneT	$(20.28\pm13.87)\times10^{04}$	$(27.47\pm19.35)\times10^{04}$	0.43
RLNU	420.06±172.51	354.73±131.36	0.36
$H_1(180°)$	$37.93\times10^{03}\pm26.03\times10^{02}$	$39.48\times10^{03}\pm31.05\times10^{02}$	0.36
$H_2(135°)$	655.51±40.19	680.15±45.56	0.34
EntT	$1.65\times10^{03}\pm0.05$	1.65±0.03	0.33
$H_1(135°)$	$39.24\times10^{03}\pm29.55\times10^{02}$	$40.97\times10^{03}\pm32.92\times10^{02}$	0.30
SRE	0.89±0.02	0.89±0.01	0.25
$\prod_1$	$2.43\times10^{03}\pm1.42$	1.70±1.44	0.25
M_4	$1.15\times10^{10}\pm2.11\times10^{09}$	$1.05\times10^{10}\pm2.48\times10^{09}$	0.23
M_2	$18.08\times10^{03}\pm33.25\times10^{02}$	$16.54\times10^{03}\pm39.11\times10^{02}$	0.23
ConT	72.89±13.11	66.84±15.39	0.23
GLNU	$11.17\times10^{03}\pm62.84\times10^{02}$	$12.57\times10^{03}\pm51.29\times10^{02}$	0.15
DM	$(34.25\pm16.98)\times10^{02}$	$(41.02\pm17.55)\times10^{02}$	0.15
ConD	$(84.78\pm41.82)\times10^{04}$	$10.11\times10^{05}\pm42.80\times10^{04}$	0.14
LBP7	18.20±4.48	19.75±5.14	0.14
HOM	0.43±0.03	0.44±0.03	0.11
CORR	$0.01\pm0.17\times10^{-02}$	$0.02\pm0.16\times10^{-02}$	0.07
LBP4	13.88±3.48	14.56±4.05	0.07
LBP1	10.01±2.52	10.15±3.03	0.06
$\prod_2$	746.63±508.99	631.55±556.24	0.06
SYM	$0.99\pm0.54\times10^{-02}$	$0.99\pm0.57\times10^{-02}$	0.01
M_1	0.42±0.85	0.38±0.84	0.00
M_3	$(27.06\pm53.97)\times10^{03}$	$(24.54\pm53.85)\times10^{03}$	0.00
RP	0.65±0.21	0.65±0.21	0.00
Feature Set B			
GSM	42.17±12.95	59.06±20.83	1.66
P_{40}	60.75±13.98	40.65±19.88	1.80
DoS	84.88±12.39	60.36±17.89	3.17

B. Classification Results

We calculated the average accuracy, PPV, sensitivity, and specificity values by using various combinations of features in different classifiers, namely, probabilistic neural network, decision tree, and SVM using different feature ranking methods. Since SVM provided higher accuracies, we have presented the results obtained using SVM alone in Table II. Among all the three feature ranking techniques, the significant features selected using the KL divergence feature ranking technique when used in the SVM classifier with the linear kernel and polynomial kernel of degree 1 resulted in the highest performance measures: sensitivity of 83.33%, specificity of 95.39%, PPV of 89.71%, and accuracy of 90.66%. It is evident that the inclusion of DoS for training effectively increases the accuracy (see Table II). Analysis shows that the inclusion of 32 features (29 from Feature Set A and 3 from Feature Set B; see Table I) in the

TABLE II
SVM CLASSIFICATION RESULTS USING FEATURES OBTAINED USING KL DIVERGENCE FEATURE RANKING METHOD

Kernel functions	No. of features	Sensitivity (%)	Specificity (%)	PPV (%)	Accuracy (%)
Feature Set A					
Linear	29	79.52	88.16	71.08	83.76
Poly1	29	79.52	88.16	71.08	83.76
Poly2	13	71.57	84.92	65.20	80.04
Poly3	19	59.40	79.22	48.77	74.35
RBF	11	64.23	77.32	41.05	74.42
Feature Set A + B					
Linear	**32**	**83.33**	**95.39**	**89.71**	**90.66**
Poly2	16	61.61	83.33	63.48	75.65
Poly3	22	86.94	88.33	71.20	87.48
RBF	14	65.28	76.32	34.93	74.38

SVM classifier gives the best sensitivity of 83.33%, specificity of 95.39%, and accuracy of 90.66%.

C. Integrated Index

The range (mean $\pm$ standard deviation) of the PRI for the symptomatic class was 1.40 ± 0.01, and that for the asymptomatic class was 21.71 ± 0.01. Thus, the index has a significantly distinct range for the two classes. The asymptomatic images have a higher value because of the presence of the *stenosis* feature (which has a lower value for the asymptomatic plaques) in the denominator of (41).

VII. DISCUSSION

Kyriacou *et al.* [14] reviewed CAD techniques for plaque characterization and classification in terms of the methods for image segmentation and denoising, morphological analysis, and plaque detection. The 61 texture and shape features from 230 plaque ROIs were classified using a modular neural network. A classification accuracy of only 73.1% was obtained [15]. Kyriacou *et al.* [16] used ten texture and morphological features in neural and statistical classifiers and obtained an accuracy of around 71.2%. In 2007, the same group [17] employed multilevel binary and grayscale morphological analyses for plaque categorization. Using pattern spectra features from 274 plaques in an SVM classifier, they obtained an accuracy of 73.7%. Seven texture and motion patterns obtained from ten symptomatic and nine asymptomatic cases were used in a fuzzy c-means classifier [18]. An accuracy of only 84% was obtained. In our previous work [19], we used texture features alone (standard deviation, entropy, symmetry, and run percentage) from plaque ROIs (150 asymptomatic and 196 symptomatic) and obtained an accuracy of only 82.4% using SVM with the RBF kernel. The aforementioned studies are limited either by low accuracies and/or by the higher number of features used.

Plaque echogenicity characteristics of 54 plaques from both classes were quantified using 21 significant first-order statistical features and Laws' texture energy. On evaluating a novel hybrid neural network, an accuracy of 99.1% was reported [20]. However, this study is limited by the smaller sample size. In 2009, our group [21] extracted 114 features (based on morphological, histogram, and Rayleigh parameters and image texture) from several image sources, namely, normalized, envelope, noiseless, and speckle images of plaques (102 asymptomatic and 44 symptomatic). We obtained an accuracy of around 99.2% using the Adaboost classifier, although at an increased computational cost due to the large number of features. Recently [22], a multiresolution approach for texture-based classification of plaques was proposed. The mean and standard deviation of the various detail subimages obtained on decomposing the images with several multiresolution-based decomposition schemes were used as features. An accuracy of 90% was obtained on using ten features based on wavelet packet transform in an SVM classifier.

In the proposed technique, we have used a unique novel powerful combination of 29 texture-based features, DoS, GSM, and $P40$ to obtain a good classification accuracy of 90.66%. The process, particularly the feature extraction part, is fast and simple due to the direct extraction of features from the plaque ROIs without a prerequisite for any complex image preprocessing or modeling. Since we have used the commonly acquired ultrasound images for classification, the technique can be afforded by any hospital. The implementation of the technique as a software application is easy, and downloading and installation do not incur any extra cost. The proposed CAD tool is robust as it has been developed using threefold stratified cross-validation technique. Hence, the classifier is reliable in classifying unseen new plaque images. The proposed novel PRI can be used in objectively assessing the nature of the plaque and in monitoring how the features vary over time. If only a few features vary significantly over a period of time, our future systems can use only those features for classification.

Even though a high accuracy has been obtained with a manageable number of features, we intend to improve it by using other features like the fractal dimension which was found to be significantly different [46]. Moreover, in this work, we have used manually delineated plaques. Even though such a task is easy for experienced radiologists and sonographers, it is difficult for less skilled personnel leading to interobserver variabilities and errors. Therefore, in future, we intend to make the plaque ROI segmentation process automatic. Since the ground truth is based on the patient's history of clinical symptoms, there is a probability of error if the patients do not accurately recollect the symptoms or when asymptomatic plaques get labeled as symptomatic when the symptoms might have actually occurred due to plaque in the heart than in the carotid artery. Moreover, some asymptomatic plaques which are in the process of becoming symptomatic tend to have the textures typical of symptomatic plaques. In such cases, our algorithm will classify them as symptomatic when the ground truth is in effect asymptomatic. This may be one of the reasons for the lower accuracy. These issues can be addressed if the ground truth is based on pathological studies.

VIII. CONCLUSION

In this paper, we have proposed a CAD technique for plaque characterization using a unique combination of texture features. We have also incorporated a classification step which classifies the plaques into symptomatic or asymptomatic with the aid of the grayscale features and the DoS. Our novel

feature combination coupled with SVM with polynomial kernel function of order 1 resulted in a good accuracy of 90.66%. Such a good accuracy, along with the fact that the technique is noninvasive, cost-effective, fast, objective, and robust, makes the technique a suitable adjunct tool for physicians to use in order to make a confident call on the nature of the plaque and, subsequently, the treatment protocol. The proposed novel PRI can also be used to objectively classify the plaques using a single-valued number and to monitor the feature variations over time. Additional studies are needed in future to establish the robustness of the proposed technique and the PRI using more databases.

REFERENCES

[1] WHO, CVD. [Online]. Available: http://www.who.int/mediacenter/factsheets/fs317/en/index.html

[2] S. Carr, A. Farb, W. H. Pearce, R. Virmani, and J. S. Yao, "Atherosclerotic plaque rupture in symptomatic carotid artery stenosis," *J. Vasc. Surg.*, vol. 23, no. 5, pp. 755–765, May 1996.

[3] T. G. Brott, R. W. Hobson, G. Howard, G. S. Roubin, W. M. Clark, W. Brooks, A. Mackey, M. D. Hill, P. P. Leimgruber, A. J. Sheffet, V. J. Howard, W. S. Moore, J. H. Voeks, L. N. Hopkins, D. E. Cutlip, D. J. Cohen, J. J. Popma, R. D. Ferguson, S. N. Cohen, J. L. Blackshear, F. L. Silver, J. P. Mohr, B. K. Lal, and J. F. Meschia, "Stenting versus endarterectomy for treatment of carotid-artery stenosis," *N. Engl. J. Med.*, vol. 363, no. 1, pp. 11–23, Jul. 2010.

[4] "MRC European Carotid Surgery Trial: Interim results for symptomatic patients with severe (70–99%) or with mild (0–29%) carotid stenosis," *Lancet*, vol. 337, no. 8752, pp. 1235–1243, May 1991.

[5] "Endarterectomy for moderate symptomatic carotid stenosis: Interim results from the MRC European Carotid Surgery Trial," *Lancet*, vol. 347, no. 9015, pp. 1591–1593, Jun. 1996.

[6] "Randomized trial of endarterectomy for recently symptomatic carotid stenosis: Final results of the MRC European Carotid Surgery Trial (ECST)," *Lancet*, vol. 351, no. 9113, pp. 1379–1387, May 1998.

[7] J. F. Polak, L. Shemanski, D. H. O'Leary, D. Lefkowitz, T. R. Price, P. J. Savage, W. E. Brant, and C. Reid, "Hypoechoic plaque at US of the carotid artery: An independent risk factor for incident stroke in adults aged 65 years or older. Cardiovascular health study," *Radiology*, vol. 208, no. 3, pp. 649–654, Sep. 1998.

[8] D. Inzitari, M. Eliasziw, P. Gates, B. L. Sharpe, R. K. Chan, H. E. Meldrum, and H. J. Barnett, "The causes and risk of stroke in patients with asymptomatic internal-carotid-artery stenosis. North American Symptomatic Carotid Endarterectomy Trial Collaborators," *N. Engl. J. Med.*, vol. 342, no. 23, pp. 1693–700, Jun. 2000.

[9] G. Geroulakos, G. Ramaswami, N. A. Nicolaides, K. James, N. Labropoulos, G. Belcaro, and M. Holloway, "Characterization of symptomatic and asymptomatic carotid plaques using high resolution real-time ultrasonography," *Br. J. Surg.*, vol. 80, no. 10, pp. 1274–1277, Oct. 1993.

[10] U. R. Acharya, O. Faust, F. Molinari, L. Saba, A. Nicolaides, and J. S. Suri, "An accurate and generalized approach to plaque characterization in 346 carotid ultrasound scans," *IEEE Trans. Instrum. Meas.*, vol. 61, no. 4, pp. 1045–1053, Apr. 2012.

[11] N. Szekely, N. Toth, and B. Pataki, "A hybrid system for detecting masses in mammographic images," *IEEE Trans. Instrum. Meas.*, vol. 55, no. 3, pp. 944–952, Jun. 2006.

[12] J. Stoitsis, S. Golemati, and K. S. Nikita, "A modular software system to assist interpretation of medical images—Application to vascular ultrasound images," *IEEE Trans. Instrum. Meas.*, vol. 55, no. 6, pp. 1944–1952, Dec. 2006.

[13] J. S. Suri, C. Kathuria, and F. Molinari, *Atherosclerosis Disease Management*. New York: Springer-Verlag, 2011.

[14] E. C. Kyriacou, C. Pattichis, M. Pattichis, C. Loizou, C. Christodoulou, S. K. Kakkos, and A. Nicolaides, "A review of noninvasive ultrasound image processing methods in the analysis of carotid plaque morphology for the assessment of stroke risk," *IEEE Trans. Inf. Technol. Biomed.*, vol. 14, no. 4, pp. 1027–1038, Jul. 2010.

[15] C. I. Christodoulou, C. S. Pattichis, M. Pantziaris, and A. Nicolaides, "Texture based classification of atherosclerotic carotid plaques," *IEEE Trans. Med. Imag.*, vol. 22, no. 7, pp. 902–912, Jul. 2003.

[16] E. Kyriacou, M. S. Pattichis, C. I. Christodoulou, C. S. Pattichis, S. Kakkos, N. Griffing, and A. Nicolaides, "Ultrasound imaging in the analysis of carotid plaque morphology for the assessment of stroke," *Stud. Health Technol. Inform.*, vol. 113, pp. 241–275, 2005.

[17] E. Kyriacou, M. Pattichis, C. S. Pattichis, A. Mavrommatis, C. I. Christodoulou, S. Kakkos, and A. Nicolaides, "Classification of atherosclerotic carotid plaques using morphological analysis on ultrasound images," *J. Appl. Intell.*, vol. 30, no. 1, pp. 3–23, Feb. 2009.

[18] J. Stoitsis, S. Golemati, K. S. Nikita, and A. N. Nicolaides, "Characterization of carotid atherosclerosis based on motion and texture features and clustering using fuzzy c-means," in *Conf. Proc. IEEE Eng. Med. Biol. Soc.*, 2004, pp. 1407–1410.

[19] R. U. Acharya, O. Faust, A. P. Alvin, S. Vinitha Sree, F. Molinari, L. Saba, A. Nicolaides, and J. S. Suri, "Symptomatic vs. asymptomatic plaque classification in carotid ultrasound," *J. Med. Syst.*, vol. 36, no. 3, pp. 1861–1871, Jun. 2012.

[20] S. G. Mougiakakou, S. Golemati, I. Gousias, A. Nicolaides, and K. Nikita, "Computer-aided diagnosis of carotid atherosclerosis based on ultrasound image statistics, Laws' texture and neural networks," *Ultrasound. Med. Biol.*, vol. 33, no. 1, pp. 26–36, Jan. 2007.

[21] J. Seabra, L. M. Pedro, F. E. Fernandes, and J. Sanches, "Ultrasonographic characterization and identification of symptomatic carotid plaques," in *Proc. 32th Annu. Int. Conf. IEEE EMBS*, Sep. 2010, pp. 6110–6113.

[22] N. N. Tsiaparas, S. Golemati, I. Andreadis, J. S. Stoitsis, I. Valavanis, and K. S. Nikita, "Comparison of multiresolution features for texture classification of carotid atherosclerosis from B-mode ultrasound," *IEEE Trans. Inf. Technol. Biomed.*, vol. 15, no. 1, pp. 130–137, Jan. 2011.

[23] T. Elatrozy, A. Nicolaides, T. Tegos, and M. Griffin, "The objective characterization of ultrasonic carotid plaque features," *Eur. J. Vasc. Endovasc. Surg.*, vol. 16, no. 3, pp. 223–230, Sep. 1998.

[24] N. Carter-Monroe, S. K. Yazdani, E. Ladich, F. D. Kolodgie, and R. Virmani, "Introduction to the pathology of carotid atherosclerosis: Histologic classification and imaging correlation," in *Atherosclerosis Disease Management*. New York: Springer-Verlag, 2011, pt. 1, pp. 3–35.

[25] M. B. Griffin, E. Kyriacou, C. Pattichis, D. Bond, S. K. Kakkos, M. Sabetai, G. Geroulakos, N. Georgiou, C. J. Dore, and A. Nicolaides, "Juxtaluminal hypoechoic area in ultrasonic images of carotid plaques and hemispheric symptoms," *J. Vasc. Surg.*, vol. 52, no. 1, pp. 69–76, Jul. 2010.

[26] O. Joakimsen, K. H. Bøona, and E. Stensland-Bugge, "Reproducibility of ultrasound assessment of carotid plaque occurrence, thickness, and morphology. The Tromsø study," *Stroke*, vol. 28, no. 11, pp. 2201–2207, Nov. 1997.

[27] A. F. Aburahma, S. P. Thiele, and J. T. Wulu, Jr., "Prospective controlled study of the natural history of asymptomatic 60% to 69% carotid stenosis according to ultrasonic plaque morphology," *J. Vasc. Surg.*, vol. 36, no. 3, pp. 437–442, Sep. 2002.

[28] T. Ojala, M. Pietikäinen, and D. Harwood, "A comparative study of texture measures with classification based on feature distributions," *Pattern Recognit.*, vol. 29, no. 1, pp. 51–59, Jan. 1996.

[29] T. Ojala, M. Pietikäinen, and T. Maenpaa, "Multiresolution gray-scale and rotation invariant texture classification with local binary patterns," *IEEE Trans. Pattern Anal. Mach. Intell.*, vol. 24, no. 7, pp. 971–987, Jul. 2002.

[30] C. V. Jawahar and A. K. Ray, "Incorporation of gray-level imprecision in representation and processing of digital images," *Pattern Recognit. Lett.*, vol. 17, no. 5, pp. 541–546, May 1996.

[31] F. Tomita and S. Tsuji, *Computer Analysis of Visual Textures*. Boston, MA: Kluwer, 1990.

[32] M. M. Galloway, "Texture Analysis Using Grey Level Run Lengths," NASA STI/Recon Technical Report N, Linthicum Heights, MD, 1974, vol. 75.

[33] A. Kadyrov and M. Petrou, "The trace transform and its applications," *IEEE Trans. Pattern Anal. Mach. Intell.*, vol. 23, no. 8, pp. 811–828, Aug. 2001.

[34] C. Nikias and A. Petropulu, *Higher-Order Spectral Analysis*. Englewood Cliffs, NJ: Prentice-Hall, 1997.

[35] K. C. Chua, V. Chandran, U. R. Acharya, and C. M. Lim, "Cardiac state diagnosis using higher order spectra of heart rate variability," *J. Med. Eng. Technol.*, vol. 32, no. 2, pp. 145–155, Mar./Apr. 2006.

[36] A. Ramm and A. Katsevich, *The Radon Transform and Local Tomography*. Boca Raton, FL: CRC Press, 1996.

[37] L. M. Pedro, M. M. Pedro, I. Gonçalves, T. F. Carneiro, C. Balsinha, R. Fernandes e Fernandes, and J. Fernandes e Fernandes, "Computer-assisted carotid plaque analysis: Characteristics of plaques associated with cerebrovascular symptoms and cerebral infarction," *Eur. J. Vasc. Endovasc. Surg.*, vol. 19, no. 2, pp. 118–123, Feb. 2000.

[38] "Beneficial effect of carotid endarterectomy in symptomatic patients with high grade carotid stenosis," *N. Engl. J. Med.*, vol. 325, no. 7, pp. 445–453, Aug. 1991.
[39] "Endarterectomy for asymptomatic carotid artery stenosis," *JAMA*, vol. 273, no. 18, pp. 1421–1428, May 1995.
[40] L. M. Pedro, J. Fernandes e Fernandes, M. M. Pedro, I. Gonçalves, N. V. Dias, R. Fernandes e Fernandes, T. F. Carneiro, and C. Balsinha, "Ultrasonographic risk score of carotid plaques," *Eur. J. Vasc. Endovasc. Surg.*, vol. 24, no. 6, pp. 492–498, Dec. 2002.
[41] J. F. Box, "Guinness, gosset, fisher, and small samples," *Stat. Sci.*, vol. 2, no. 1, pp. 45–52, 1987.
[42] M. Bressan and J. Vitria, "On the selection and classification of independent features," *IEEE Trans. Pattern Anal. Mach.Intell.*, vol. 25, no. 10, pp. 1312–1317, Oct. 2003.
[43] R. Duda, P. Hart, and D. Stork, *Pattern Classification*, 2nd ed. New Delhi, India: Wiley India, 2007.
[44] V. David and A. Sanchez, "Advanced support vector machines and kernel methods," in *Neurocomputing*. Amsterdam, The Netherlands: Elsevier, 2003.
[45] K. R. Muller, S. Mika, G. Ratsch, K. Tsuda, and B. Scholkopf, "An introduction to kernel based learning algorithms," *IEEE Trans. Neural Networks*, vol. 12, no. 2, pp. 181–201, Mar. 2001.
[46] P. Asvestas, S. Golemati, G. K. Matsopoulos, K. S. Nikita, and A. N. Nicolaides, "Fractal dimension estimation of carotid atherosclerotic plaques from B-mode ultrasound: A pilot study," *Ultrasound Med. Biol.*, vol. 28, no. 9, pp. 1129–1136, Sep. 2002.

U. Rajendra Acharya is currently a visiting faculty in Ngee Ann Polytechnic, Singapore. He is also an Adjunct Professor in the University of Malaya, Malaysia, and the Singapore Institute of Technology–University of Glasgow, Singapore; an associate faculty in SIM University, Singapore; and an adjunct faculty in the Manipal Institute of Technology, Manipal, India.

M. Muthu Rama Krishnan received the Ph.D. degree from the Indian Institute of Technology, Kharagpur, India.

He is currently a Research Engineer with Ngee Ann Polytechnic, Singapore. His research interest includes medical image analysis and pattern classification.

S. Vinitha Sree is currently a visiting scientist at Global Biomedical Technologies Inc., Roseville, CA. Her areas of interest include medical data mining, breast imaging systems, and health-care systems and management. She has published over 38 peer-reviewed publications.

João Sanches is currently a Professor with the Bioengineering Department at the Instituto Superior Tecnico, Lisboa, Portugal, and a Researcher at the Institute for Systems and Robotics. His work has been focused in biomedical signal and image processing and physiological modeling of biological systems.

Dr. Sanches is a senior member of EMBS and a Technical Committee member of the IEEE Signal Processing Society.

Shoaib Shafique completed General Surgery training at Yale New Haven Hospital, then completed Vascular Fellowship at the Indiana University School of Medicine, Indianapolis, and then completed advanced endovascular training at Arizona Heart Institute and Hospital, Phoenix.

He is currently an Attending Vascular Surgeon with CorVasc MDs, Indianapolis.

Andrew Nicolaides received the M.S. degree from the Royal College of Surgeons of England, London, U.K., and the F.R.C.S. and F.R.C.S.E. degrees from the Royal College of Surgeons of England, London, and the Royal College of Surgeons of Edinburgh, Midlothian, U.K., in 1967.

He is currently a Professor Emeritus at Imperial College, London. He is the coauthor of more than 500 original papers and editor of 14 books.

Luís Mendes Pedro received the M.D. and the Ph.D. degrees from the Medical School of the University of Lisbon, in 1987 and 1993, respectively.

He is currently an Associate Professor and a Consultant of Vascular Surgery with the Cardiovascular Institute and the Lisbon University Medical School, Hospital de Santa Maria, Lisbon, Portugal. His main interests are ultrasound plaque characterization, carotid surgery, and endovascular surgery.

Jasjit S. Suri is an innovator, a visionary, a scientist, and an internationally known world leader. He is currently the Chief Technology Officer with AtheroPoint LLC, Roseville, CA, and is also affiliated with the Department of Biomedical Engineering, Idaho State University, Pocatello, ID.

Dr. Suri was crowned with the Director General's Gold Medal in 1980 and the Fellow of the American Institute of Medical and Biological Engineering, awarded by the National Academy of Sciences, Washington, DC, in 2004. He has been the Chairman of the IEEE Denver section, has won over 50 awards during his career, and has held executive positions.